THE ASTRONOMICAL JOURNAL, 171:210 (14pp), 2026 April
https://doi.org/10.3847/1538-3881/ae448e

# A Narrowband Technosignature Search toward the Hycean Candidate K2-18 b Using the VLA and MeerKAT

C. D. Tremblay[1,2,3,4], S. Chaudhary[5], M. G. Li[6], S. Z. Sheikh[1,2], T. Myburgh[7,1], D. Czech[2], D. E. MacMahon[2], P. B. Demorest[4], R. A. Donnachie[7,1], A. P. V. Siemion[1,8], V. Gajjar[1], M. Lebofsky[2], K. Wandia[9], K. I. Perez[1], and N. Madhusudhan[10]

[1] SETI Institute, 339 Bernardo Avenue, Suite 200, Mountain View, CA 94043, USA
[2] Berkeley SETI Research Center, University of California, Berkeley, CA 94720, USA
[3] Department of Physics and Astronomy, University of New Mexico, Albuquerque, NM 87131, USA
[4] National Radio Astronomy Observatory, 1003 Lopezville Road, Socorro, NM 87801, USA
[5] Indian Institute of Science Education and Research, Mohali, India
[6] Department of Earth, Planetary, and Space Sciences, University of California, Los Angeles, CA 90024, USA
[7] Mydon Solutions (Pty) Ltd., 102 Silver Oaks, 23 Silverlea Road, Wynberg, Cape Town 7800, South Africa
[8] Breakthrough Listen, University of Oxford, Department of Physics, Denys Wilkinson Building, Keble Road, Oxford OX1 3RH, UK
[9] Jodrell Bank Centre for Astrophysics, University of Manchester, Manchester M13 9PL, UK
[10] Institute of Astronomy, University of Cambridge, Madingley Road, Cambridge CB3 0HA, UK

*Received 2025 December 11; revised 2026 January 28; accepted 2026 February 9; published 2026 March 9*

## Abstract

K2-18 b, a sub-Neptune exoplanet located in the habitable zone of its host star, has emerged as an important target for atmospheric characterization, and assessments of potential habitability. Motivated by recent interpretations of JWST observations suggesting a hydrogen-rich atmosphere consistent with Hycean-world scenarios, we conducted a coordinated, multiepoch search for narrowband radio technosignatures using the Karl G. Jansky Very Large Array equipped with the COSMIC backend and the MeerKAT telescope with the BLUSE backend. Our observations span frequencies from 544 MHz to 9.8 GHz and include multiple epochs that cover at least one full orbital period of the planet. In this work we outline, create, and apply a comprehensive postprocessing framework that incorporates observatory-informed radio frequency interference masking, drift-rate filtering based on the expected dynamics of the K2-18 system, multibeam spatial discrimination, primary and secondary transit filtering (when applicable), and signal-to-noise-ratio-based excision of weak and strong spurious signals. Across all bands and epochs, no signals consistent with an astrophysical or artificial origin were identified at a limit of $10^{12}$–$10^{13}$ W. These nondetections allow us to place upper limits on the presence of persistent, isotropic narrowband transmitters within the K2-18 system, providing the first interferometric technosignature constraints for a Hycean-planet candidate. Our results demonstrate the efficacy of coordinated multiepoch interferometric searches and establish a methodological framework for future technosignature studies of nearby potentially habitable exoplanets.

*Unified Astronomy Thesaurus concepts:* GPU computing (1969); Astrobiology (74); Search for extraterrestrial intelligence (2127); Exoplanets (498)

## 1. Introduction

K2-18 b, a sub-Neptune exoplanet located within the habitable zone of its host star, presents a compelling opportunity to investigate the atmospheric composition and potential habitability of planets beyond our solar system. With an estimated mass of $8.63 \pm 1.35\,M_?$, a radius of $2.61 \pm 0.09\,R_?$, and an equilibrium temperature between 250 and 300 K (B. T. Montet et al. 2015; P. Sarkis et al. 2018; B. Benneke et al. 2019; R. Cloutier et al. 2019), K2-18 b may possess conditions suitable for liquid water (N. Madhusudhan et al. 2020). Atmospheric studies using transmission spectra from the James Webb Space Telescope (JWST) indicate the presence of substantial $CH_4$ and $CO_2$, while showing a lack of $NH_3$ and stratospheric $H_2O$ (N. Madhusudhan et al. 2023). These findings are consistent with theoretical models predictions (e.g., R. Hu et al. 2021; S.-M. Tsai et al. 2021) for Hycean worlds—planets characterized by deep, stable oceans beneath hydrogen-rich atmospheres (N. Madhusudhan et al. 2021). Such a chemical composition raises intriguing questions regarding the planet's potential habitability and the persistence of surface oceans (E. F. L. Barrier & N. Madhusudhan 2025; R. Hu et al. 2025).

Thus, K2-18 b serves as an important benchmark for studies of sub-Neptune atmospheres and their potential habitability. At the same time, it highlights the importance of cautious interpretation when analyzing transmission spectra of planets orbiting magnetically active stars (e.g T. Barclay et al. 2021). Ongoing and future observations with JWST and complementary facilities are expected to further constrain the planet's atmospheric structure, composition, and dynamics, providing key insights into Hycean worlds and the broader search for habitable environments beyond Earth and potential hosts for atmospheric biosignatures.

Although the potential for biosignatures in K2-18 b's atmosphere remains tentative (e.g., N. Madhusudhan et al. 2023, 2025; L. Pica-Ciamarra et al. 2025; L. Welbanks et al. 2025), another way to constrain the planet's habitability is to consider the search for technosignatures—observable indicators of advanced technology within or near the planetary

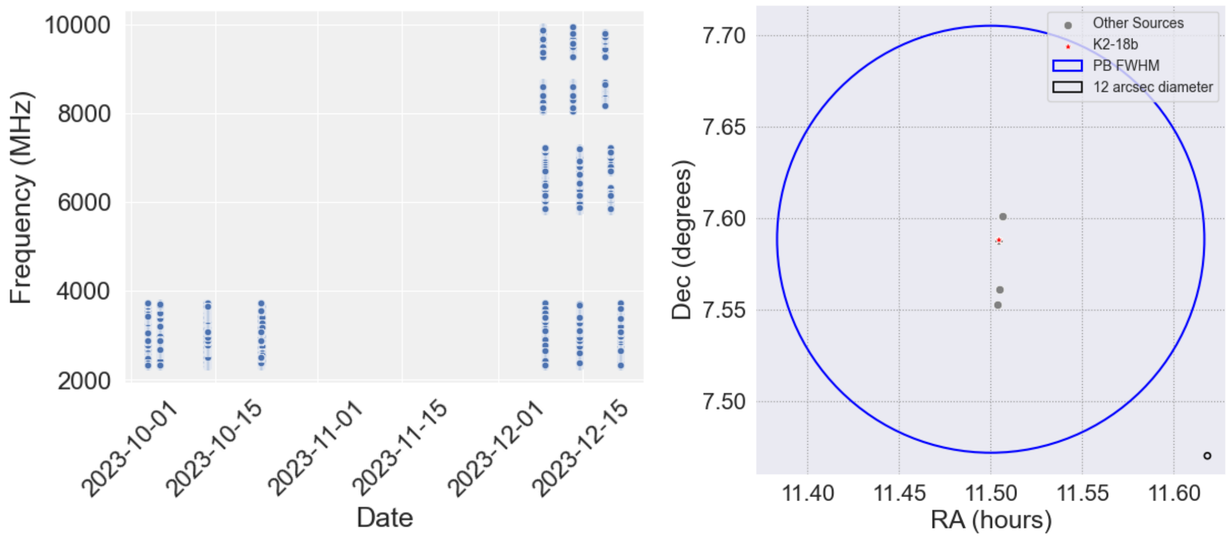

**Figure 1.** The observed sources and data collected during the K2-18 b observing campaign with the Commensal Open-Source Multi-Mode Interferometer Cluster (COSMIC). Left: the dates of the observations and the frequencies in which signals were detected. Right: the locations of the four coherent beams (gray circles), the position of K2-18 (red star), and the FWHM primary beam (PB) for the COSMIC telescope at *S* band.

system. The leakage radiation from the Earth consists of a large fraction of narrowband signals ($\ll$500 Hz) and, in addition, narrowband signals are ideal beacons (G. Cocconi & P. Morrison 1959; J. T. Wright et al. 2022; S. Z. Sheikh et al. 2025). Additionally, since almost 80% of Earth's leakage from powerful radar signals, such as the Deep Space Network, is located in the ecliptic plane (P. Fan et al. 2025), there is a high probability that when looking at the ecliptic planes of other systems, the chance of detection of a technosignature increases. To distinguish genuine extraterrestrial signals from terrestrial radio frequency interference (RFI), we leverage the planet's orbital motion and stellar occultation events: for example, true signals from K2-18 b would exhibit predictable Doppler drift rates and any emission should vanish when the planet passes behind its host star.

To explore this possibility, we have undertaken a coordinated observing campaign with the MeerKAT radio telescope in South Africa and the National Science Foundation's Karl G. Jansky Very Large Array (VLA) in New Mexico. This observing program spans frequencies from 544 MHz to 9.8 GHz and multiple epochs, covering at least one full orbital period of K2-18 b. This is in addition to the campaign completed at the Allen Telescope Array in California (R. C. Saide et al. 2023). These observations aim to search for narrowband technosignatures while simultaneously advancing our understanding of the atmospheric and environmental properties of the planet. In addition to the observations, in this work we provide a framework for the postprocessing of observations toward other exoplanetary systems.

## 2. Observations

### 2.1. VLA-COSMIC

We observed the K2-18 planetary system and its host star using the VLA. Observations were conducted over multiple epochs, spaced up to 1 week apart, between 2023 September 29 and 2023 December 21 (Project Code: VLA/23B-307), as shown in Figure 1. The dates of the observations for each band are summarized in Table 1 and the parameters for the real-time processing are outlined in Table 2.

**Table 1**
Summary of Observations toward K2-18 b

| Telescope | Band | Obs. Date (YYYY-MM-DD) | Obs. Time (UTC) | Orbital Phase ($\phi$)[a] |
|---|---|---|---|---|
| VLA | *S* | 2023-10-03 | 19:50–20:00 | 0.76 |
| VLA | ⋯ | 2023-10-05 | 20:28–20:38 | 0.82 |
| VLA | ⋯ | 2023-10-13 | 15:03–15:13 | 0.06 |
| VLA | ⋯ | 2023-10-22 | 14:26–14:36 | 0.33 |
| VLA | ⋯ | 2023-12-08 | 17:31–17:41 | 0.76 |
| VLA | ⋯ | 2023-12-14 | 10:49–10:59 | 0.94 |
| VLA | ⋯ | 2023-12-21 | 08:29–08:39 | 0.15 |
| VLA | *C* | 2023-12-08 | 17:01–17:11 | 0.76 |
| VLA | ⋯ | 2023-12-14 | 10:18–10:28 | 0.94 |
| VLA | ⋯ | 2023-12-19 | 15:44–15:54 | 0.09 |
| VLA | *X* | 2023-12-08 | 10:02–10:12 | 0.75 |
| VLA | ⋯ | 2023-12-13 | 09:25–09:35 | 0.90 |
| VLA | ⋯ | 2023-12-19 | 16:43–16:53 | 0.10 |
| MeerKAT | UHF[b] | 2023-09-30 | 11:13–11:18 | 0.66 |
| MeerKAT | *L* | 2023-10-01 | 11:03–11:08 | 0.69 |
| MeerKAT | *S4* | 2023-10-06 | 08:48–08:53 | 0.84 |

**Notes.**
[a] Calculated from B. Benneke et al. (2019), where $T_0 = 57725.051189$ MJD (UTC) for the midtransit ($\phi = 0$).
[b] Ultrahigh frequency (UHF) band.

Data were collected simultaneously using both the COSMIC backend (C. D. Tremblay et al. 2024) and the standard WIDAR correlator system (R. Perley 2004). For the standard WIDAR data, the correlator was configured in 8 bit mode with a 2 GHz bandwidth and operated in continuum mode with 2 MHz wide coarse channels. These data were analyzed for radio emission from the host; no detections were made for either the coherent or incoherent emission (K. Wandia et al. 2026).

**Table 2**
Parameters for the COSMIC and BLUSE Observations and Real-time Pipeline

| Telescope | Band | Date (YYYY-MM-DD) | Integration Time (s) | Threshold ($\sigma$) | Channel Width (Hz) | No. of Antennas | Recording[a] (bits) | Polarizations |
|---|---|---|---|---|---|---|---|---|
| VLA | *S* | 2023-10-03 | 56 | 10 | 2 | 17 | 8 | 2 |
| VLA | *S* | 2023-10-05 | 56 | 10 | 2 | 23 | 8 | 2 |
| VLA | *S* | 2023-10-13 | 56 | 10 | 2 | 24 | 8 | 2 |
| VLA | *S* | 2023-10-22 | 56 | 10 | 2 | 22 | 8 | 2 |
| VLA | *S* | 2023-12-08 | 56 | 10 | 2 | 25 | 8 | 2 |
| VLA | *S* | 2023-12-14 | 56 | 10 | 2 | 25 | 8 | 2 |
| VLA | *S* | 2023-12-21 | 56 | 10 | 2 | 23 | 8 | 2 |
| VLA | *C* | 2023-12-08 | 56 | 10 | 2 | 25 | 8 | 2 |
| VLA | *C* | 2023-12-14 | 56 | 10 | 2 | 25 | 8 | 2 |
| VLA | *C* | 2023-12-19 | 56 | 10 | 2 | 25 | 8 | 2 |
| VLA | *X* | 2023-12-08 | 56 | 10 | 2 | 25 | 8 | 2 |
| VLA | *X* | 2023-12-13 | 56 | 10 | 2 | 25 | 8 | 2 |
| VLA | *X* | 2023-12-19 | 56 | 10 | 2 | 25 | 8 | 2 |
| MeerKAT | UHF | 2023-09-30 | 290 | 10 | 1 | 64 | 10 | 2 |
| MeerKAT | *L* | 2023-10-01 | 290 | 10 | 1 | 64 | 10 | 2 |
| MeerKAT | *S4* | 2023-10-06 | 290 | 10 | 1 | 64 | 10 | 2 |

**Note.**
[a] For both 8 bit and 10 bit recordings, quantization losses are negligible for the sensitivity limits considered in this work.

The COSMIC system is designed to operate in parallel with most VLA observations, recording data passively without direct control over the observing frequency or pointing. For this program, however, we were awarded 6 hr of Director's Discretionary Time (Proposal VLA/23B-307). During these observations, we recorded up to 1.2 GHz of bandwidth across three frequency ranges: 2.4–3.6 GHz (*S* band), 5–7.2 GHz (*C* band), and 8.1–9.8 GHz (*X* band). Over the course of the campaign, the source was observed seven times in *S* band and three times each in *C* and *X* band. For each epoch, the source was observed for a total of 10 minutes, with each 56 s segment independently processed and searched for narrowband signals. See Figure 1 for an outline of the dates and frequency coverage of the observations, and the placement of the four coherent beams in the field.

### 2.1.1. Calibration and Real-time Processing

The COSMIC system employs a real-time data-processing pipeline that performs calibration, channelization, beam forming, and searches for narrowband signals. A detailed description of this pipeline is provided in C. D. Tremblay et al. (2024, 2025); a brief summary is given here. The pipeline is controlled through an observing script that defines the triggers for the experiment (e.g., observation ID, project code, and frequency range) and instructs the system when to record and how to process the data. When an observation is triggered, the VLA software assigns an observation intent[11] that initiates either a correlation and calibration sequence or a technosignature search mode.

During the calibration phase, the data are divided into 32 fragments of 1 MHz each and distributed across processing nodes, where correlation is performed using the XGPU software correlator. Complex gain solutions are then derived for each frequency segment. The results are returned to the head node, where the data are reordered by frequency and a calibration quality assessment is completed. Real-time RFI flagging is also performed, and gain solutions are smoothed over flagged 1 MHz channels. The final gain solutions are applied to the field-programmable gate arrays, enabling automatic phase calibration of incoming target-field data.

## 2.2. MeerKAT-BLUSE

We conducted single-epoch observations in each frequency band toward K2-18 using the MeerKAT telescope in South Africa with the commensal backend, Breakthrough Listen User Supplied Equipment (BLUSE; D. Czech et al. 2021, 2026, in preparation). The observations were performed on 2023 September 30 at UHF (544–1015 MHz), 2023 October 1 at *L* band (900–1670 MHz), and 2023 October 6 at *S4* (2625–3500 MHz). A summary of the observations and dates is listed in Table 1 and the parameters for the real-time processing are outlined in Table 2.

BLUSE is an autonomous commensal SETI survey system. It ingests and processes packetized raw voltage data (coarse channels) directly from MeerKAT's F-engines via Ethernet multicast groups. Ordinarily, it operates in an autonomous commensal fashion, configuring itself to process the incoming data for any observing mode selected by the primary observer. It selects up to 64 targets of interest that happen to fall within the primary field of view (FOV), channelizes the data to ∼1 Hz resolution, forms synthesized beams on the targets, and conducts a narrowband technosignature search for each beam (SETICORE,[12] similar to COSMIC).

For this experiment, however, BLUSE was allocated primary telescope time (Director's Discretionary Time Proposal ID: DDT-20230920-DC-01) in a "semicommensal" mode, an approach designed to use telescope time efficiently by leveraging BLUSE's ability to operate alongside any configuration selected by a primary observer. BLUSE can record up to 290 s worth of MeerKAT's full bandwidth before its buffers are full and it needs to spend time processing the data. Therefore, a small amount of primary BLUSE telescope time was appended to the beginning of several primary

---

[11] A full list of the observations intents are noted on the NRAO website: https://www.aoc.nrao.edu/~cwalker/sched/INTENTs.html.

[12] https://github.com/lacker/seticore

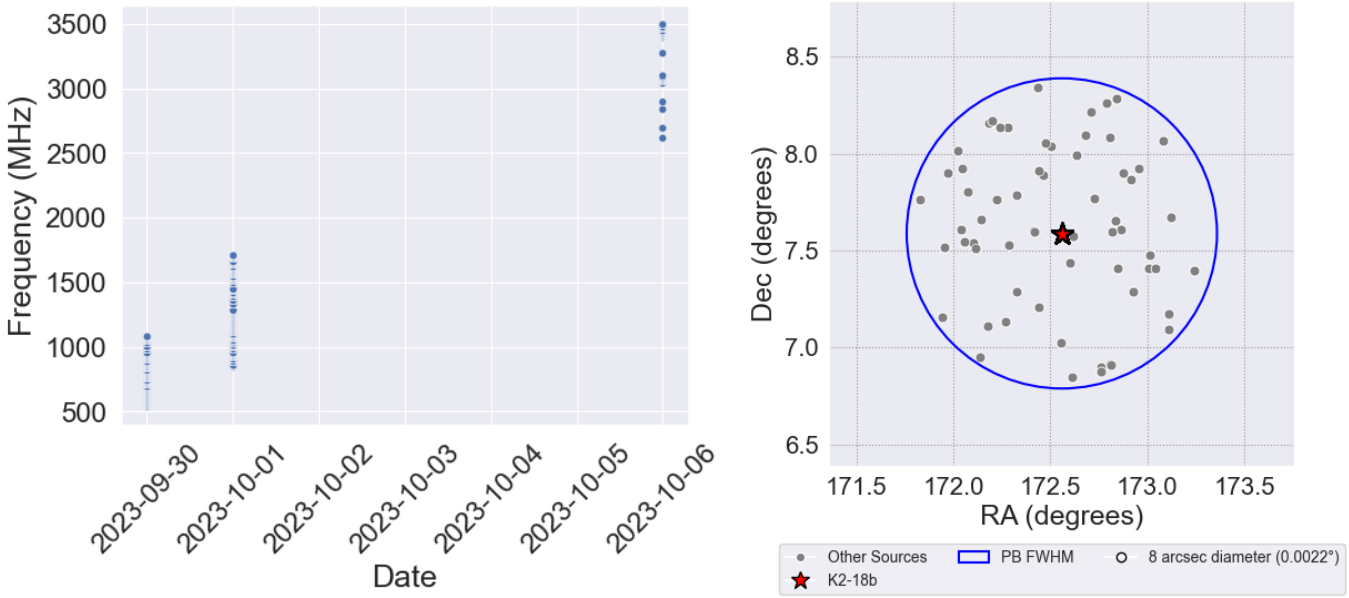

**Figure 2.** The observed sources and data collected during the K2-18 b observing campaign. Left: the dates of the observations and the frequencies in which signals were detected. Right: the locations of the 64 coherent beams (gray circles), the position of K2-18 (red star), and the FWHM PB for the MeerKAT telescope at *L* band.

observations: MeerKAT was configured and the data calibrated for the primary observation, but was directed to observe K2-18 for 5 minutes prior to the start of the primary observation.

This approach allowed BLUSE to record, process, and store additional data products (which take considerably longer to write to disk but allow later flexibility during analysis) at leisure without occupying further primary telescope time. Since BLUSE is able to operate alongside all primary telescope modes, it was easy to find suitable primary observations in UHF, *L*, and *S* band. See Figure 2 for the observations and the layout of the 64 coherent beams within the telescope's FOV during the *L*-band observation.

### 2.3. Technosignature Candidate Search

To search for narrowband signals, the pipeline fine channelized the data from the coarse channels into fine-frequency bins using a fast Fourier transform (FFT)—2 Hz for COSMIC and ~1 Hz for BLUSE.[13] The COSMIC system forms up to four coherent beams and an incoherent sum across the FOV, while MeerKAT forms 64 coherent beams. The VLA observations for this project were conducted during the array's transition from the A configuration (36 km baselines) to the D configuration (1 km baselines); consequently, the synthesized beam size varied between epochs. Given the planet's radius of 2.34 $R_\oplus$ and a distance of 38 pc, the entire K2-18 planetary system, including its host star, lies well within a single coherent beam of both telescopes.

For both facilities, a Taylor-tree dedispersion algorithm implemented in the SETICORE software package was used to identify narrowband drifting signals within the real-time pipelines. The output of the search consists of a series of metadata entries stored in an SQL database, along with calibrated voltage files for each antenna centered on the detected signals (hits). The resulting data products were then filtered to identify candidate technosignatures originating from the K2-18 system.

## 3. Postprocessing Methodology

The primary goal of this project is to search for evidence of technological activity within the K2-18 planetary system. We assess this possibility by examining whether signals detected by the real-time pipeline are spatially coincident with the planet's position on the sky, exhibit the expected Doppler drift rates, and vanish when the planet passes behind its host star during secondary transit. The following section describes in detail the procedure used to filter the signals detected by the real-time pipelines to identify the most promising technosignature candidates and is summarized in Figure 3

### 3.1. Remove Known Sources of Radio Frequency Interference

In this work, we employ multiple techniques to identify and mitigate sources of persistent RFI. For most of the frequency bands observed with both telescopes, we rely on observatory-provided data products. The NRAO supplies updated RFI plots for each configuration and observing semester, derived from time-averaged spectra in 128 MHz partitions.[14] In addition, a table of known strong RFI sources is provided, enabling us to exclude channels containing the most powerful emitters.

The South African Radio Astronomy Observatory (SARAO) provides similar information for the MeerKAT telescope,[15] though regularly updated reference plots are not yet available.

For this analysis, we generated a separate `.csv` file for each frequency band and each telescope, specifying the start and end frequencies of all identified RFI sources and, when available, the identifier for the RFI. We then excluded all detections overlapping with these frequency intervals,

---

[13] The exact frequency resolution changes depending on the primary configuration.

[14] https://science.nrao.edu/facilities/vla/docs/manuals/obsguide/rfi

[15] https://skaafrica.atlassian.net/wiki/spaces/ESDKB/pages/305332225/Radio+Frequency+Interference+RFI

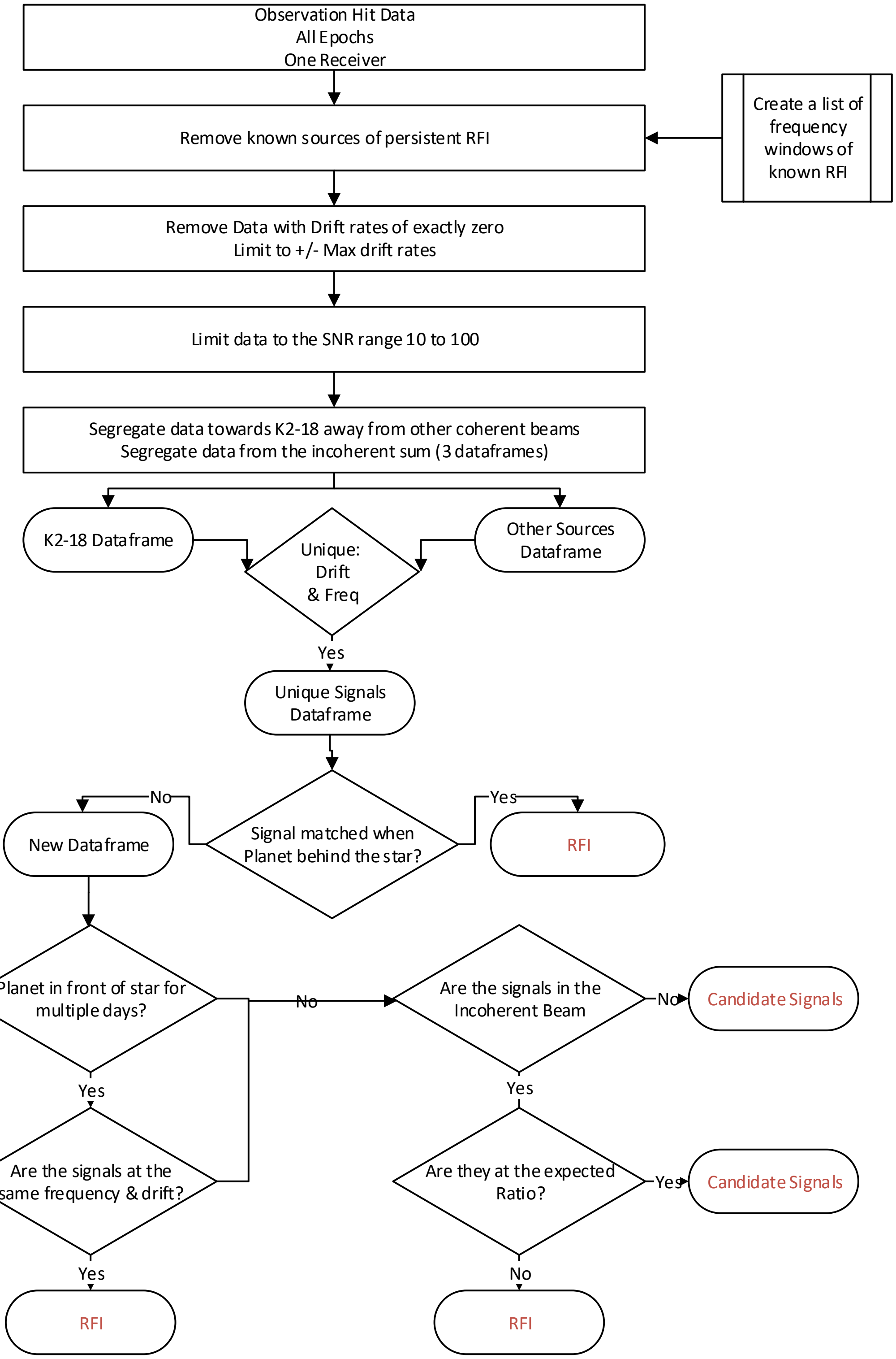

**Figure 3.** A block diagram summarizing the steps listed in Section 3 of the paper to filter the RFI discovered by the pipeline to find potential technosignature candidates.

independent of pointing direction. Figures 4 and 5 illustrate this process, showing the known RFI regions for each band and telescope along with the detection of the all the signals from COSMIC and BLUSE.

An exception to this procedure was made for the *S*-band (2–4 GHz) observations with the VLA. For these data, we used the `.csv` file produced in C. D. Tremblay et al. (2025), which was generated from time-averaged observations of a calibrator using an identical instrumental setup. This file incorporates both the persistent RFI detected by COSMIC and the supplementary information available through the NRAO RFI database.

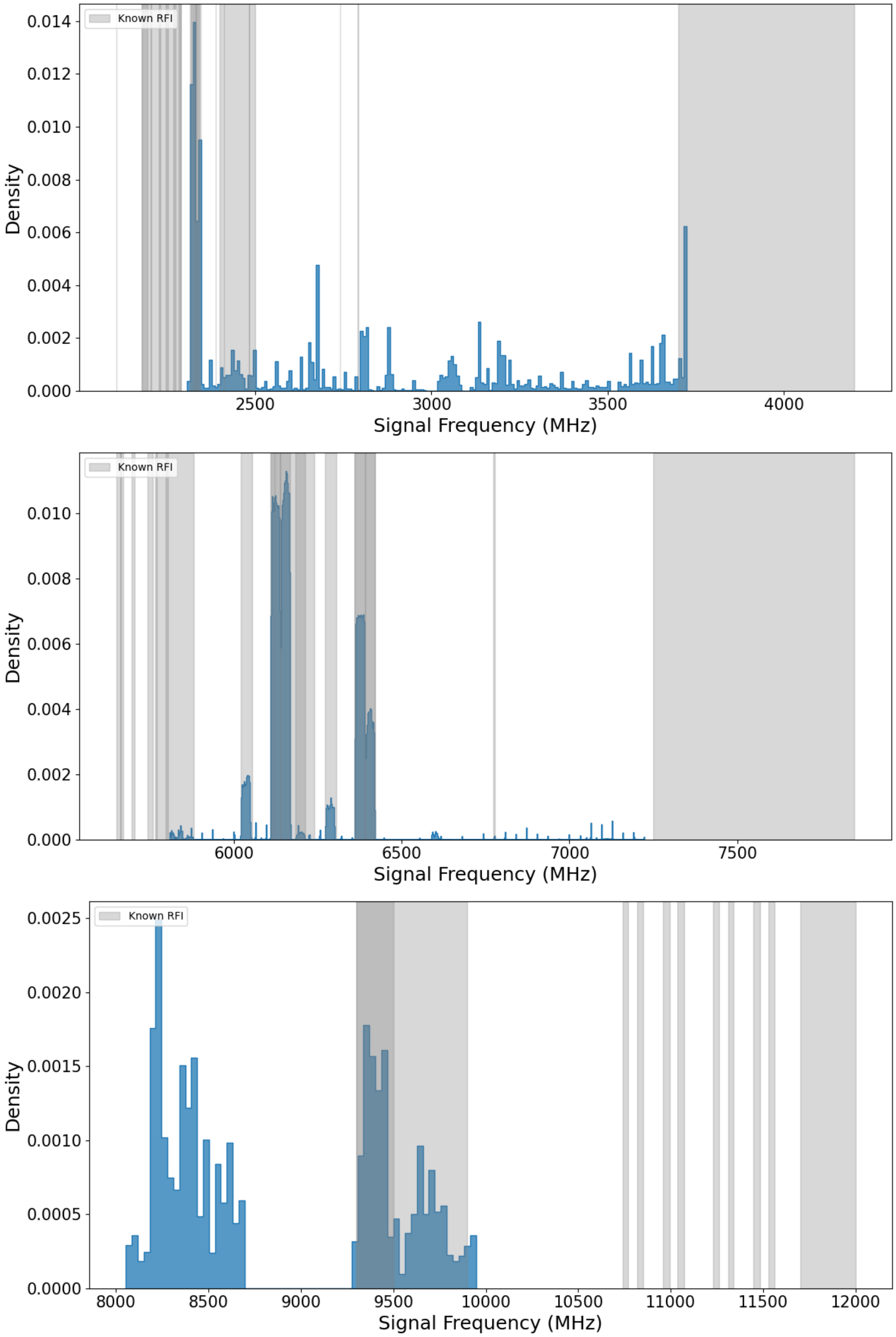

**Figure 4.** Histogram density plots of all the signals detected through the autonomous real-time pipeline running on COSMIC at the VLA prior to RFI rejection. The plots show the data from *S* band (top), *C* band (middle), and *X* band (bottom) representing all signals from all of the epochs of observations.

### *3.2. Drift Rates*

If radio emissions from K2-18 b were to be detected, the planetary signal would exhibit a Doppler drift resulting from the relative acceleration between the transmitter and the receiver. This drift manifests as a change in the observed frequency over time, caused by the combination of the planet's orbital motion around its host star and the rotational velocity of the Earth. Following the methods described by J.-K. Li et al. (2022) and M. G. Li et al. (2023), we estimate that 99% of

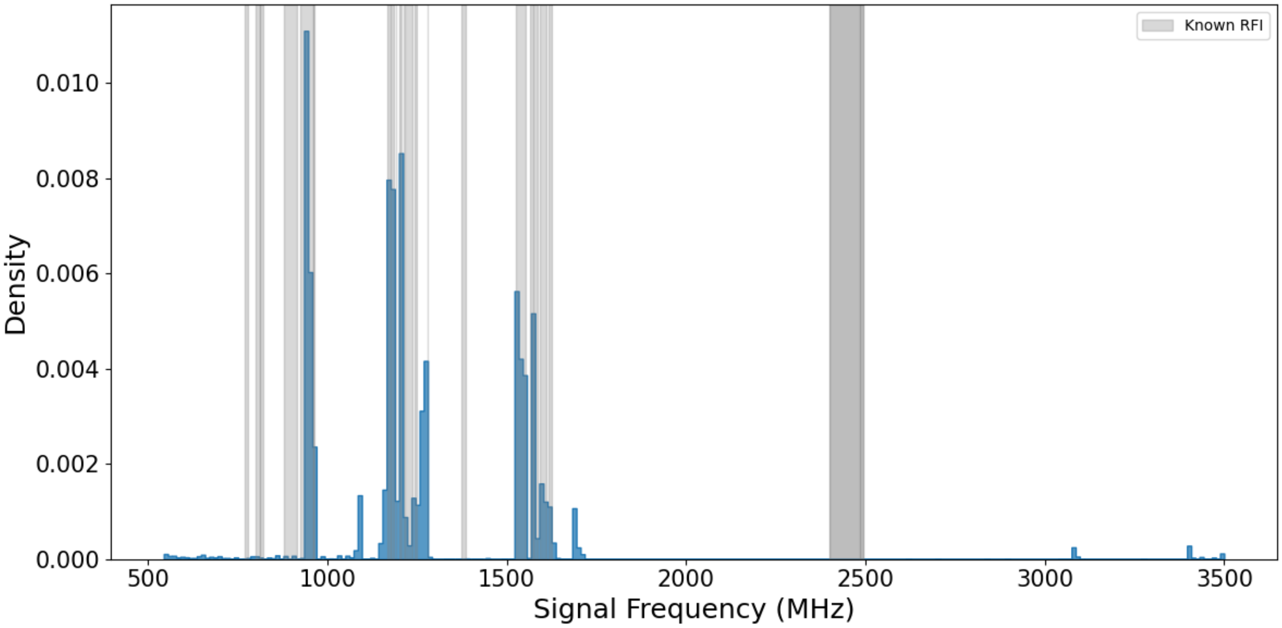

**Figure 5.** Histogram density plots of all the signals detected through the autonomous real-time pipeline running on BLUSE prior to RFI rejection. The plots show the data from all bands and from all of the epochs of observations. The gray regions show the RFI outlined in the MeerKAT online documentation.

such signals would experience a frequency drift of approximately 0.4 Hz $s^{-1}$ for signals between 544 and 1500 MHz, increasing to 1.879 Hz $s^{-1}$ near 4.5 GHz, and reaching a maximum of 4.177 Hz $s^{-1}$ around 10 GHz. These limits were adopted as search boundaries in our analysis.

As an additional filtering step, all signals with a drift rate of exactly 0 Hz $s^{-1}$ were removed, as such detections likely correspond to local RFI, where the transmitter and receiver are either stationary relative to one another or moving too slowly to produce a measurable Doppler shift within our drift-rate resolution.

### *3.3. Strong and Weak Signal Excision*

We investigated the expected false-positive rate by injecting synthetic signals into recorded data using the SETIGEN[16] package and processing the resulting datasets with the SETICORE software, employing the same drift-rate and signal-to-noise ratio (SNR) parameters as used in the real-time search (N. Steigler et al. 2026, in preparation), which highlight a similar trend as discussed in C. Choza et al. (2024). The results indicate that, on average, nearly 80% of signals with an SNR of $8\sigma$ and fewer than 64 time samples were false positives—cases in which the pipeline reported a detection despite the absence of a signal in the dynamic spectrum. This was dominated by random bright pixels aligning and the dedrifted power spectrum showing a peak. Consequently, we adopted a lower SNR threshold of $10\sigma$ for the COSMIC data, consistent with the native detection limit used in the BLUSE pipeline.

At the opposite extreme, any Earth-like civilization's radio technosignature signal traversing the ∼124 lt-yr between Earth and K2-18 b would potentially be weak. However, powerful transmitters could exist, but a more overarching consideration is antenna-generated RFI or artifacts. To assist in determining an upper limit we analyzed 1000 stamps at random containing a mix of signals from the COSMIC pipeline, which revealed that over 90% of high-SNR detections were caused by instrumental effects—appearing only in a single antenna but with a high SNR—and were not consistent with sky-dependent sources. The real-time pipeline identifies these signals in the beamformed data as the signal can reach up to $3000\sigma$ meaning that it is present in the computed data products. Therefore, we imposed an SNR upper limit of 100 during this postprocessing step but note that the original data detected by the pipeline are still present when a better algorithm for this type of artifact is developed.

In summary, we applied an SNR range of 10–100 to exclude both low-significance detections and spurious high-SNR events arising from strong RFI or instrumental artifacts. This will produce a limitation of detecting signals from K2-18 b no brighter than $10^{14}$ W for COSMIC and $10^{13}$ W for BLUSE.

### *3.4. Multibeam Analysis*

As shown in the right panels of Figures 1 and 2, we simultaneously formed multiple coherent beams toward nearby Gaia stars within the telescope's FOV. This configuration allows us to determine whether a detected signal is spatially localized to K2-18 b or instead represents RFI, which would appear in all beams at the same frequency and drift rate.

Because fine channelization is performed using an FFT, some detected signals may span multiple frequency bins if they are broader than a single channel width. To account for this, we apply a tolerance of ±1 fine channels when crossmatching detections. For COSMIC, which operates with a 2 Hz frequency resolution, this corresponds to a ±2 Hz tolerance. For MeerKAT, the search was completed at a 1 Hz resolution and a 1 Hz tolerance.

We apply a similar tolerance to the drift rate to account for standard errors in the pipeline. The SETICORE algorithm searches along all possible drift trajectories to identify the drift rate that maximizes the signal intensity, as described by C. Choza et al. (2024). For broad or nonlinearly varying

---

[16] https://setigen.readthedocs.io/en/main/

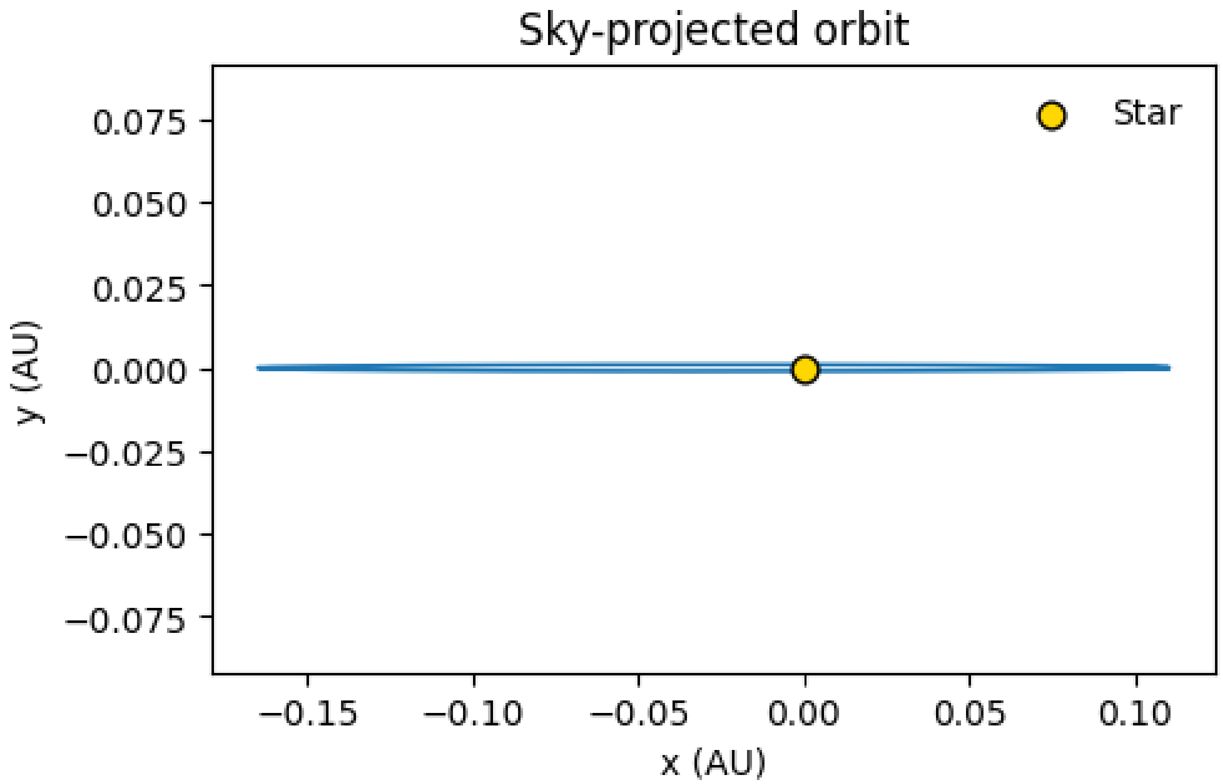

**Figure 6.** A plot showing an example model of the orbital motion of K2-18 b using the parameters listed in the NASA Exoplanet Archive. This shows that the orbit is highly eccentric ($e = 0.2$) and the transit duration is 2.66 hr. The periastron is $-5°$ so the projection introduces a nonzero mean velocity (a constant offset).

signals, the derived drift rate can differ by approximately one drift step. Consequently, we adopt a tolerance of one drift step when evaluating whether detections correspond to the same signal across multiple sky positions.

### 3.5. Primary and Secondary Transits

K2-18 b is a sub-Neptune-sized exoplanet located approximately 38 pc away, residing within the habitable zone of its host star and orbiting with a period of 33 days. We used the NASA Exoplanet Archive Transit Viewer[17] to determine the epochs of both primary and secondary transits. (See Figure 6 to see a model of the orbit of the planet around the star.) Based on the model from B. Benneke et al. (2019), secondary transits were predicted to occur on 2023 September 25 at 00:35, October 27 at 23:09, November 29 at 21:43, and 2024 January 1 at 20:16 (UTC). Primary transits were predicted on 2023 September 7, October 11, November 13 at 10:26, and December 16 at 08:15 (UTC). After secondary transit, the planet is occulted (superior conjunction) by its host star for approximately 2.7 hr, meaning that a transmitter located on or near the planet would be visible to the telescope for 99.6% of its orbital period.

When applicable, we compared signals detected while the planet was behind the star (secondary transit) to those observed when the planet was in front of the star. Any signal detected during the secondary transit, and immediately after while the planet is obscured from view, cannot originate from a transmitter on or near the planet's surface. Although it is theoretically possible for an unrelated transmitter to exist elsewhere within the system and remain out of phase with the planet, that scenario lies beyond the scope of this analysis. Using the tolerances described in Section 3.4, we identify signals exhibiting matching frequencies and drift rates while the planet is obscured by the star and when it can be observed from Earth. We retain only those detections that were unique to the planet's visible phase and excluded all others from the candidate list.

We note that for these observations, data were not taken while K2-18 b was occulted by its star. Therefore, this step is not applicable for these observations. However, as this paper also provides a framework for future observations, we have left this step as an additional filter for signals of interest.

### 3.6. Multiple Day Comparison

When multiple observations are obtained on different days while the planet is in front of its host star, we also compare the detected signals across epochs. As described by J.-K. Li et al. (2022), signals transmitted from a moving source (e.g., a planet's surface) and received by a moving observer (e.g., a ground-based telescope) will experience a changing observed frequency and drift rate over time. For sufficiently long observations, the frequency evolution of such a drifting signal is expected to trace a sinusoidal pattern. Consequently, if the same source is observed on multiple days, we do not expect the signal to appear at an identical frequency or drift rate. Any detection exhibiting the same frequency and drift rate across different epochs is therefore most likely due to RFI or instrumental systematics.

Conversely, a signal that is unique in both frequency and drift rate represents the strongest technosignature candidate.

---

[17] https://exoplanetarchive.ipac.caltech.edu/cgi-bin/TransitView

**Table 3**
Summary Table of Results from Filtering the Data from Both COSMIC and BLUSE

| Step | VLA |  |  | MeerKAT |  |  |
|---|---|---|---|---|---|---|
|  | *S* band 2–4 GHz | *C* band 4–8 GHz | *X* band 8–12 GHz | UHF 0.544–1.015 GHz | *L* band 0.9–1.670 GHz | S4 band 2.625–3.5 GHz |
| Initial | 10,743,382 | 9,920,694 | 310,961 | 59,030 | 398,867 | 4712 |
| Step 3.1: RFI | 6,737,277 | 237,333 | 178,944 | 59,030 | 118,677 | 4712 |
| Step 3.2: Drift Rates | 589,011 | 31,517 | 18,974 | 5902 | 58,734 | 1488 |
| Step 3.3: Strong and weak signals | 384,955 | 19,816 | 11,067 | 2991 | 13,386 | 1103 |
| Toward K2-18 b | 141,450 | 4911 | 242 | 46 | 225 | 180 |
| Step 3.4: Multibeam | 13,847 | 768 | 0 | 0 | 0 | 0 |
| Step 3.5: Transits | N/A | N/A | N/A | N/A | N/A | N/A |
| Step 3.6: Day | 4316 | 86 | ⋯ | N/A | N/A | N/A |
| Step 3.7: Beam | 0 | 0 | ⋯ | N/A | N/A | N/A |
| Step 3.8: Visual | 0 | 0 | ⋯ | ⋯ | ⋯ | ⋯ |

**Note.** The numbers are the remaining signals after each step explained in Section 3 are completed. The row “Toward K2-18 b” represents the number of signals unique to that sky position after the first three steps of filtering were completed. We use “N/A” to denote any steps that are considered by not applicable for this set of data. The frequency bands listed represent the nominal receiver coverage. The exact subbands observed are described in the relevant sections of the text.

### 3.7. Coherent and Incoherent Beam Comparison

The data generated by forming a coherent beam are targeted toward a specific source. However, an incoherent beam is the sum across the entire telescope’s FOV, removing the ability to localize a signal. A signal detected in both a coherent and an incoherent beam is possible, however, a signal of the same origin in the incoherent beam will have a reduced sensitivity determined by the calculation

$$\mathrm{SNR}_{\mathrm{coherent}} \leqslant \sqrt{N_{\mathrm{antennas}}} \times \mathrm{SNR}_{\mathrm{incoherent}}. \tag{1}$$

However, signals that are not of the same origin, although having a similar frequency and drift rate, will not follow this relationship. Therefore, this is a strong delineator of RFI within the field and emission emanating from a target source.

### 3.8. Visual Inspection

For our strongest technosignature candidates, we plot the dynamic spectrum and visually inspect the signals. Candidate technosignatures will be those that have passed through all of the above filters, appear in all online antennas in the array, and show a distinct linear signal drifting in time and frequency.

## 4. Results

For each telescope and receiver band the data were processed sequentially through the steps outlined in Section 3. A summary of the results is found in Table 3. The observations with MeerKAT did not include an incoherent beam or multiepoch analysis. Therefore, those steps are marked as “N/A.” For observations with both the VLA and MeerKAT the observation dates did not include when the planet was obscured by the star, so therefore that row in the table is also marked as “N/A.” Below we provide a more detailed analysis of each set of observations.

### 4.1. COSMIC S-band Search

All detected signal hits across the seven observing epochs were loaded, each containing frequency, SNR, drift rate, and time metadata. Known RFI frequency ranges were imported from a `.csv` file, and a mask was applied to exclude contaminated bands. Hits with SNR $>$ 100 were removed to avoid instrumental artifacts, reducing the dataset to ∼385,000 detections and resulting in only 3.5% of the original detections remaining for analysis (Figure 4). This subset contained coherent, nonzero-drift signals within plausible Doppler ranges and moderate SNR values—characteristics consistent with expected astronomical rather than terrestrial origins. Unlike the other observation completed with the VLA, we observed K2-18 b in *S* band in seven different epochs on 2023 October 3, 2023 October 5, 2023 October 13, 2023 October 22, 2023 December 8, 2023 December 14, and 2023 December 21. In all instances the source was visible from Earth.

The filtered data were divided into three groups: signals detected toward K2-18 b, those from other field sources detected in coherent beams, and signals detected in the incoherent sum. Candidates that are unique to the coherent beam toward K2-18 b were identified by requiring frequency differences greater than ±2 Hz and drift-rate differences exceeding ±0.1 Hz s$^{-1}$ relative to all other detections, resulting in 13,847 unique signals.

Finally, these detections were classified by date using the `tstart` time stamp. After analysis, 663 candidates matched between the incoherent and coherent beams, however, none showed an expected power ratio (4.69) for a real astrophysical signal. After applying all remaining filters described in Section 3, no viable technosignature candidates were identified.

### 4.2. COSMIC C-band Search

The COSMIC system recorded observations of K2-18 b over three consecutive weeks on 2023 December 8, 14, and 19 at frequencies between 5 and 7.2 GHz, resulting in 9,920,694 detected hits. Each observation consisted of 10 minutes on source, divided into 56 s segments that were searched independently. Data for December 8 and 14 were obtained after K2-18 b was out of secondary transit, whereas observations for December 19 occurred shortly after primary transit on December 16. However, at no time during these observations was the planet obscured from view. A histogram of the hits detected by the real-time pipeline is shown in Figure 4.

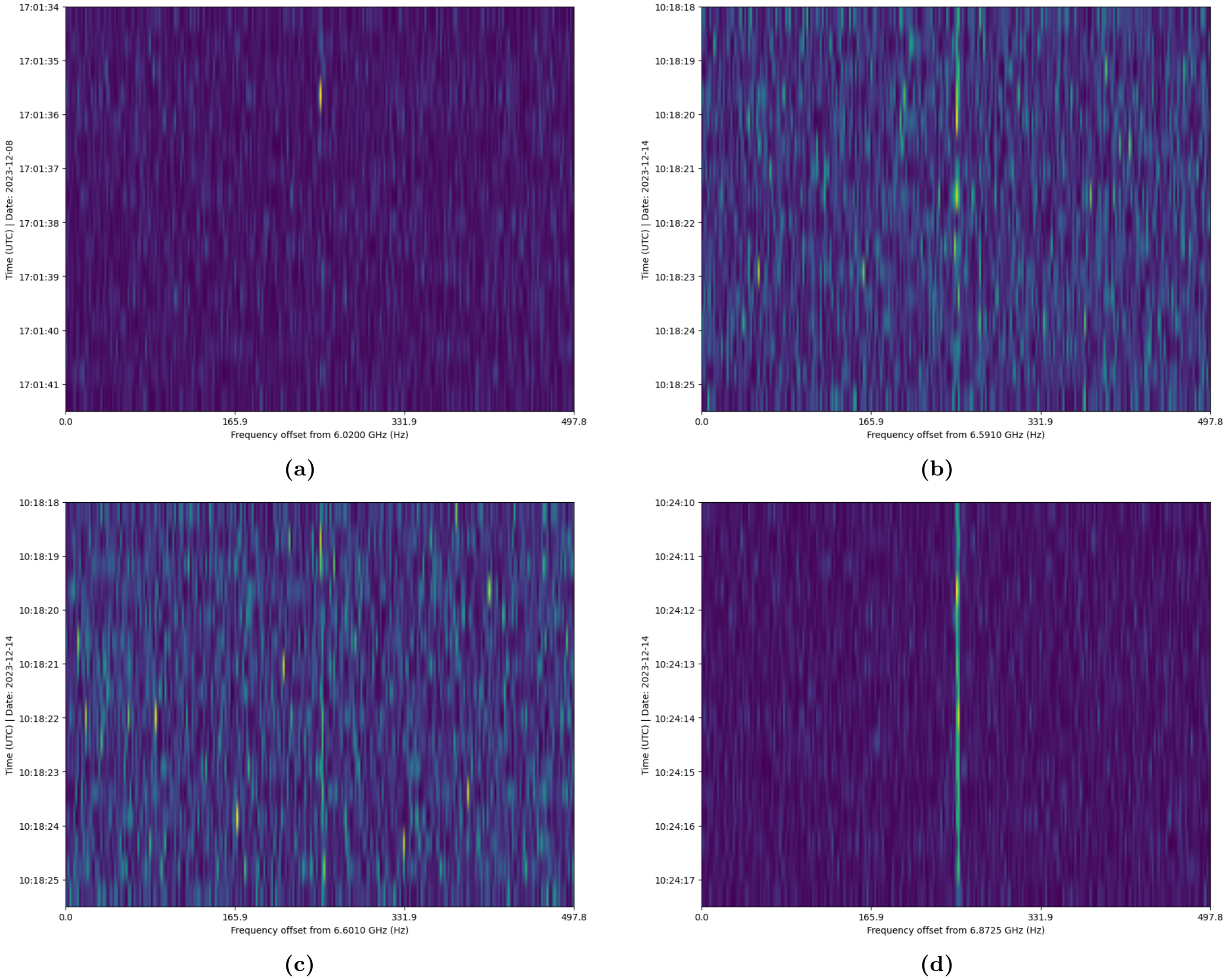

(a) (b)

(c) (d)

**Figure 7.** Dynamic spectra of four signals visualized after they passed through the criteria listed in the pipeline. All signals were found to be RFI or an instrument artifact. (a) Spectra showing a bright pixel with a weak drifting signal. The signal was not present in all antennas. (b) A weak signal drifting in time and frequency was an inconsistent intensity. The signal was not present in all antennas. (c) An example weak signal in a noisy part of the spectrum and surrounded by RFI. (d) A bright drifting signal only present in one antenna, representing a instrument artifact.

In the first stage of processing, the known RFI frequency bins were removed using a predefined mask and the remaining signals were filtered as described in Section 3. After applying drift-rate limits of $\pm 1.9\,\mathrm{Hz\,s^{-1}}$ and restricting detections to those with $10 \leqslant \mathrm{SNR} \leqslant 100$, fewer than 5000 candidate signals toward K2-18 b remained. Of those signals, no signals had a match between the incoherent beam and the coherent beam from Step 3.7, so all remaining signals from the coherent beam were searched for a comparison of signals between each of the 3 days of observations (Step 3.6). Following the postprocessing pipeline, 86 signals were retained for visual inspection using the stamp files. The dynamic spectra for each remaining signal had similar drift rates and angles. Of these remaining signals, 90% of the signals were within a megahertz of each other around 6.6 GHz. The spectra for each antenna showed inconsistency (not present in all antennas and not present in all time bins), suggesting that all remaining signals were RFI instead of a signal originating from the K2-18 system. Dynamic spectra of four examples of the remaining signals, all found to be RFI or telescope artifacts, are shown in Figure 7.

### 4.3. *COSMIC X-band Search*

Similarly to the *C*-band observations, the COSMIC system recorded additional data over three consecutive weeks on 2023 December 8, 14, and 19. These observations were conducted across the same four coherent beams, each targeting different sources within the FOV, including K2-18 b. In total, the real-time pipeline detected 310,961 hits over these three epochs. Each observation consisted of 10 minutes on source, divided into 56 s segments that were independently calibrated, beam formed, and searched for narrowband drifting signals.

Following the postprocessing workflow described in Section 3, all detections were first crossmatched against known RFI frequency bins, and hits located within contaminated bands were removed. The remaining signals were filtered based on drift rate, retaining only those within $\pm 4.2\,\mathrm{Hz\,s^{-1}}$ and with an SNR between 10 and 100. After applying these constraints, 242 hits remained that were unique to the position of K2-18 b.

These 242 candidate detections were then examined for spatial consistency across the four coherent beams by comparing their appearance and intensity. A genuine technosignature would be expected to appear only in the beam corresponding to the K2-18 b position and not in the off-target data. However, after this comparison, no surviving signals exhibited spatial isolation or consistent drift-rate behavior, indicative of an astrophysical or artificial origin. As a result, no technosignature candidates were identified in the observations.

### 4.4. MeerKAT Ultrahigh Frequency

Because the BLUSE observations in the UHF band were conducted on a single day, we relied primarily on the spatial filtering afforded by the backend's 64 coherent beams to distinguish RFI from potential technosignatures. Each beam targeted a different position on the sky drawn from a catalog of nearby stellar systems, including K2-18 b. This configuration allows local interference to be recognized through its appearance in multiple beams, whereas an astrophysical signal would be confined to only one.

Across the observing period, the real-time detection system reported 59,030 hits within the 544–1015 MHz band. Drift rates ranged from $-10$ to $+9$ Hz s$^{-1}$, with ≈83% of detections exhibiting zero drift, consistent with stationary terrestrial emitters. After applying the masking procedure described in Section 3 and discarding signals outside the allowed drift-rate window, we further restricted the dataset to detections with an SNR between 10 and 100, leaving 5.1% of the initial hit set.

A final spatial comparison required that any surviving detection appear exclusively in the K2-18 b beam and in none of the other 63 beams. No signals met this criterion and no viable technosignature candidates were identified in the UHF dataset.

### 4.5. MeerKAT L Band

For the *L*-band observations, the BLUSE system again synthesized 64 coherent beams across the MeerKAT field, each directed toward a unique entry in the predefined target catalog. This multibeam strategy provides strong spatial discrimination against RFI, as genuine extraterrestrial transmitters are expected to appear in only a single beam.

The BLUSE pipeline identified 398,867 initial detections during the *L*-band session. Masking frequencies associated with persistent RFI reduced the sample to 118,677 detections. Imposing the standard drift-rate constraint of $\pm 1.9$ Hz s$^{-1}$ further reduced the set to 58,734 signals, and limiting the selection to $10 \leqslant \mathrm{SNR} \leqslant 100$ yielded 13,386 hits appropriate for spatial analysis.

Prior to crossmatching these detections across all 64 coherent beams, 225 signals appeared solely in the K2-18 b beam. However, no signals toward K2-18 b were unique when compared to the other 63 coherent beams, so no further analysis was required.

### 4.6. MeerKAT S Band

The real-time pipeline detected a total of 4712 hits across the *S4* observing band. None of these overlapped with frequencies flagged in the catalog of persistent RFI, and thus no detections were removed at this preliminary stage.

Applying the nominal drift-rate constraint of $\pm 1.9$ Hz s$^{-1}$ reduced the dataset to 1488 signals, and further restricting the sample to detections with $10 \leqslant \mathrm{SNR} \leqslant 100$ yielded 1103 hits for spatial comparison. Each of these was examined for exclusivity to the beam centered on K2-18 b.

No detections were found to be unique to the K2-18 b beam; all surviving signals were either coincident across multiple beams or exhibited characteristics indicative of RFI. As a result, no technosignature candidates were identified in the *S*-band observations.

**Table 4**
Equivalent Isotropic Radio Power Limits for K2-18 b for Each Receiver Band Observation

| Telescope | Band | Frequency Range (MHz) | EIRP Limit ($10^{12}$ W) |
|---|---|---|---|
| MeerKAT | UHF | 544–1015 | 1.6 |
| MeerKAT | *L* | 900–1670 | 1.2 |
| MeerKAT | *S4* | 2625–3500 | 1.1 |
| VLA | *S* | 2500–3500 | 23 |
| VLA | *C* | 5800–7200 | 16 |
| VLA | *X* | 8000–9800 | 13 |

**Note.** EIRP limits correspond to the minimum detectable isotropic transmitter power at the distance of K2-18 b, using the sensitivity of each observing band and assuming narrowband emission. See the Appendix for details on the calculation.

## 5. Discussion

### 5.1. Constraints on Technosignatures in the K2-18 System

We have conducted a coordinated, multiepoch search for narrowband technosignatures toward the K2-18 system using two interferometric facilities: the VLA with the COSMIC backend and the MeerKAT array with the BLUSE backend. Complementary analyses of our VLA observations show no coherent or incoherent stellar radio emission from K2-18 and place microjansky-level upper limits on its magnetic activity (K. Wandia et al. 2026). After applying a sequence of filters based on RFI excision, drift-rate constraints, multibeam spatial localization, primary transit behavior, and SNR thresholds, no viable technosignature candidates were identified in any band or epoch.

This null result allows us to place upper limits on continuously emitting, narrowband transmitters within the K2-18 system. At a distance $d_{\mathrm{p}} = 38$ pc,[18] the sensitivities achieved in our observations imply that any isotropic transmitter located on or near K2-18 b and emitting between 544 MHz and 9.8 GHz must have an equivalent isotropic radio power (EIRP) below the limits derived in this work (see Section 3 and Table 4). All of these values are close to or less than the power provided by the Arecibo telescope ($\sim 10^{13}$ W; A. P. V. Siemion et al. 2013) and put stringent constraints on the system. These constraints apply to transmitters that are narrowband (a few hertz wide), persistent on timescales comparable to our integration times, and emitting such that the Earth lies within the beam pattern during the epochs observed. Intermittent, broadband, or highly directional signals that did not illuminate the Earth at those times are not ruled out by this study.

Although we do not detect technosignatures, these limits contribute to the growing set of observational constraints on technologically active civilizations around nearby stars and

---

[18] https://exoplanetarchive.ipac.caltech.edu/overview/K2-18

represent one of the first targeted searches toward a Hycean-planet candidate.

### 5.2. *Implications for K2-18 b and Hycean Worlds*

K2-18 b is an important benchmark for studies of sub-Neptune atmospheres and Hycean-world scenarios. Atmospheric inferences from JWST suggest a hydrogen-rich atmosphere with $CH_4$ and $CO_2$ and a lack of $NH_3$ and CO, with important implications for a water-rich interior and a possible Hycean world (N. Madhusudhan et al. 2023; S. Howard et al. 2025; R. Hu et al. 2025). As outlined in detail by J. T. Wright et al. (2022), our radio observations provide an independent constraint. Within the narrowband, low-drift parameter space probed here, we find no evidence for technologically generated radio emission from the K2-18 system.

This result is consistent with several possibilities: K2-18 b may be uninhabited, it may host pretechnological life, or any technologically capable civilization may employ communication modalities that are not detectable with our current observing strategy (e.g., nonradio, broadband, low-duty cycle, or highly encrypted signals). Thus, the absence of a detection should not be interpreted as evidence against habitability or against the presence of technological activity in any absolute sense. Rather, it constrains a specific class of transmitters: persistent, narrowband emitters in the observed frequency range.

Nevertheless, combining atmospheric characterization with direct technosignature limits is valuable. K2-18 b illustrates how detailed exoplanet atmospheric studies and radio technosignature searches can be coordinated, particularly for systems in or near the habitable zone. As more Hycean candidates are identified, similar joint strategies will help place such systems in a broader comparative context.

### 5.3. *Methodological Considerations and the Role of Interferometers*

A key outcome of this work is the demonstration of a general postprocessing framework for interferometric technosignature searches. Our approach integrates (1) real-time calibration, channelization, beam forming, and drift-rate searches via COSMIC and BLUSE; (2) observatory-informed and empirically derived RFI masks; (3) multibeam spatial filtering to distinguish localized sky signals from field-wide interference; (4) drift-rate filtering based on the expected dynamics of the K2-18 system; and (5) orbital-phase-based filtering using primary and secondary transits.

Although this is not the first study toward exoplanets (R. C. Saide et al. 2023; S. Z. Sheikh et al. 2023; R. A. W. Barrett et al. 2025), the multibeam capability used in this paper is particularly important. A genuine signal from the K2-18 system is expected to appear in a single coherent beam, with an amplitude consistent with the incoherent sum (Section 3.7), whereas local RFI often appears in multiple beams and does not satisfy the expected coherent-to-incoherent SNR relation. This spatial discrimination, combined with transit-based and multiepoch consistency checks, substantially reduce the false-positive rate that was built using the framework published in N. Tusay et al. (2024) but modified to account for the larger number of coherent beams distributed across each telescope's FOV.

These techniques are not specific to K2-18 b. The framework can be applied to other exoplanetary systems observed with commensal interferometric backends and is readily scalable to larger target samples. As widefield interferometers and digital backends become more prevalent, such multibeam, multiepoch strategies will play an increasingly central role in radio technosignature searches.

### 5.4. *Limitations and Future Prospects*

Several limitations of this study should be noted. First, although our observations span at least one orbital period, they sample only a small fraction of the planet's possible orbital phases and any potential transmission strategies. Low-duty-cycle or phase-specific transmitters could be missed. Second, the search parameter space is restricted to approximately linear drift rates within the ranges motivated by the expected accelerations of the K2-18 system; signals with strongly nonlinear or rapidly varying frequency evolution may not be efficiently recovered. Third, while our RFI models combine observatory information and empirical masking, they are necessarily incomplete. Some low-level or intermittent interference may remain, and conservative masking can exclude regions in which genuine signals might reside.

Future work can address these limitations in several ways. Additional observations of K2-18 b with improved temporal sampling and broader frequency coverage would increase sensitivity to intermittent or phase-dependent transmissions. Incorporating polarization information, more flexible drift models, and machine learning–based anomaly detection into the pipeline may enhance sensitivity to nonstandard signal morphologies. Finally, applying the methods developed here to a larger sample of targets—particularly other nearby Hycean candidates and habitable-zone planets—will help place the K2-18 limits in a statistical context.

### 5.5. *Broader Context*

Technosignature searches remain exploratory, but carefully designed null results provide meaningful constraints on the prevalence and characteristics of technologically active civilizations. For K2-18 b, we present the first interferometric search of this system for narrowband radio emission over a wide frequency range, complementing ongoing atmospheric studies and establishing a template for future coordinated campaigns.

As next-generation facilities such as the Square Kilometre Array (SKA) and next-generation VLA (ngVLA) come online, the strategies used here—multibeam searches, transit- and drift-aware filtering, and systematic postprocessing—will be essential for scaling technosignature searches to larger datasets and higher sensitivities. K2-18 b thus serves both as a scientifically compelling target and as a test case for the methodologies required in future large-scale searches for technosignatures.

## 6. Conclusion

In this work, we conducted a coordinated, multifacility search for narrowband technosignatures in the K2-18 system using the VLA COSMIC and MeerKAT BLUSE backends, spanning 544 MHz to 9.8 GHz and covering multiple epochs across one orbital period of K2-18 b. Using a uniform postprocessing framework that incorporated observatory-informed RFI excision, drift-rate filtering based on the planet's orbital dynamics, multibeam spatial discrimination, cross-epoch consistency checks, and primary and secondary transit constraints, we identified no signals consistent with an artificial origin. All surviving detections were attributable to terrestrial RFI or instrumental systematics.

These nondetections enable the first expansive search for interferometric technosignature limits for a proposed Hycean-world candidate. The absence of persistent narrowband emission at our achieved sensitivities places upper limits on isotropic transmitters within the K2-18 system and demonstrates the value of combining independent arrays, backend architectures, and observing strategies.

The methodology presented here establishes a generalizable framework for future targeted searches of potentially habitable exoplanets with current and next-generation facilities such as the ngVLA and SKA. Continued multiepoch, multiband observations of nearby sub-Neptunes will further refine technosignature constraints, complement atmospheric studies, and expand the parameter space in which we can meaningfully search for technological activity beyond the solar system.

## Acknowledgments

The authors gratefully acknowledge the foundational support from John and Carol Giannandrea that made COSMIC possible. As part of the Breakthrough Listen project, the BLUSE system on the MeerKAT telescope is sponsored by Breakthrough Initiatives, an organization affiliated with the Breakthrough Prize Foundation. The National Radio Astronomy Observatory is a facility of the National Science Foundation operated under a cooperative agreement with Associated Universities, Inc. The MeerKAT telescope is operated by the South African Radio Astronomy Observatory, which is a facility of the National Research Foundation, an agency of the Department of Science and Innovation. This work has made use of the "MPIfR *S*-band receiver system" designed, constructed, and maintained by funding of the MPI für Radioastronomy and the Max-Planck-Society.

## Data Availability

All data were collected via commensal backends on the VLA and MeerKAT telescopes and are under the ownership of Breakthrough Listen and the SETI Institute. The voltage, filterbank, or database information can be made available upon request to the authors. It is our plan in the future to make these data publicly available through a web service.

*Facilities:* VLA, MeerKAT.

*Software:* astropy (Astropy Collaboration et al. 2013, 2018), pandas (T. pandas development team 2020), seaborn (M. L. Waskom 2021).

## Appendix
## Sensitivity Limit Calculation

In both the COSMIC and BLUSE experiments the signals are searched for in beam-formed data. Therefore, the sensitivity limits, when no signals originating from the planet are detected, are carefully considered. To set the flux density limit ($S_{\rm limit}$) we use the standard equation for beam-formed data:

$$S_{\rm limit} = \frac{\rm SEFD}{B_e\sqrt{n_{\rm pol} \times n \times t_{\rm int} \times \Delta\nu}} \times {\rm SNR}. \tag{A1}$$

The system equivalent flux density (SEFD) is determined using the standard radiometer equation and limits published on both the NRAO[19] website for COSMIC and the SARAO[20] website for BLUSE, and is shown in Equation (A2). The values of $S_{\rm limit}$ are in janskies and are converted using the definition of 1 Jy is equal to $1 \times 10^{-26}$ W m$^{-2}$ Hz$^{-1}$:

$$\mathrm{SEFD} = \frac{2k_{\rm B}T_{\rm sys}}{A_{\rm eff}}. \tag{A2}$$

The beamformer efficiency value ($B_e$) is determined through observations on each system. In C. D. Tremblay et al. (2024), we determined the beamformer efficiency on COSMIC using a methanol maser to be between 0.85 and 0.95 depending on the day. For BLUSE, we used observations of the signals from JWST to determine a beamformer efficiency of 0.93. Therefore, we use a value of $B_e$ of 0.9 for COSMIC and 0.93 for BLUSE.

The values for the number of polarizations ($n_{\rm pol}$), the number of antennas ($n$), the integration time ($t_{\rm int}$), SNR as the threshold of the experiment, and the bandwidth ($\Delta\nu$) are from Table 2. These values will potentially change per each experiment. We use the bandwidth of a single channel width, as we are looking for a signal that is constrained to a single channel.

To compare our limits to other technosignature surveys and to what these sensitivity limits mean for the detection of a transmitter, we use the equation for the EIRP:

$$\mathrm{EIRP} = 4\pi \mathrm{F}_{\rm min} \times D^2. \tag{A3}$$

The value $D$ is the distance to the planet in meters. The value $F_{\rm min}$ is the $S_{\rm limit}$ times the single channel bandwidth (or spectral resolution).

## ORCID iDs

C. D. Tremblay https://orcid.org/0000-0002-4409-3515
M. G. Li https://orcid.org/0000-0002-3012-4261
S. Z. Sheikh https://orcid.org/0000-0001-7057-4999
T. Myburgh https://orcid.org/0000-0003-0804-9362
D. Czech https://orcid.org/0000-0002-8071-6011
D. E. MacMahon https://orcid.org/0000-0001-6950-5072
P. B. Demorest https://orcid.org/0000-0002-6664-965X
R. A. Donnachie https://orcid.org/0009-0001-8677-372X
A. P. V. Siemion https://orcid.org/0000-0003-2828-7720
V. Gajjar https://orcid.org/0000-0002-8604-106X
M. Lebofsky https://orcid.org/0000-0002-7042-7566
K. Wandia https://orcid.org/0000-0003-4338-2611
K. I. Perez https://orcid.org/0000-0002-6341-4548
N. Madhusudhan https://orcid.org/0000-0002-4869-000X

## References

Astropy Collaboration, Robitaille, T. P., Tollerud, E. J., et al. 2013, A&A, 558, A33

Astropy Collaboration, Price-Whelan, A. M., Sipőxz, B. M., et al. 2018, AJ, 156, 123

Barclay, T., Kostov, V. B., Colón, K. D., et al. 2021, AJ, 162, 300

---

[19] https://science.nrao.edu/facilities/vla/docs/manuals/oss/performance/sensitivity

[20] https://skaafrica.atlassian.net/wiki/spaces/ESDKB/pages/277315585/MeerKAT+specifications

Barrett, R. A. W., Tremblay, C. D., Price, D. C., Green, J. A., & Addison, B. C. 2025, PASA, 42, e089
Barrier, E. F. L., & Madhusudhan, N. 2025, MNRAS, 544, 4098
Benneke, B., Wong, I., Piaulet, C., et al. 2019, ApJL, 887, L14
Choza, C., Bautista, D., Croft, S., et al. 2024, AJ, 167, 10
Cloutier, R., Astudillo-Defru, N., Doyon, R., et al. 2019, A&A, 621, A49
Cocconi, G., & Morrison, P. 1959, Natur, 184, 844
Czech, D., Isaacson, H., Pearce, L., et al. 2021, PASP, 133, 064502
Fan, P., Wright, J. T., & Lazio, T. J. W. 2025, ApJL, 990, L1
Howard, S., Helled, R., Bergermann, A., & Redmer, R. 2025, A&A, 703, A154
Hu, R., et al. 2021, ApJL, 921, L8
Hu, R., Bello-Arufe, A., Tokadjian, A., et al. 2025, arXiv:2507.12622
Li, J.-K., Zhao, H.-C., Tao, Z.-Z., Zhang, T.-J., & Xiao-Hui, S. 2022, ApJ, 938, 1
Li, M. G., Sheikh, S. Z., Gilbertson, C., et al. 2023, AJ, 166, 182
Madhusudhan, N., Nixon, M. C., Welbanks, L., Piette, A. A. A., & Booth, R. A. 2020, ApJL, 891, L7
Madhusudhan, N., Piette, A. A. A., & Constantinou, S. 2021, ApJ, 918, 1
Madhusudhan, N., Sarkar, S., Constantinou, S., et al. 2023, ApJL, 956, L13
Madhusudhan, N., Constantinou, S., Holmberg, M., et al. 2025, ApJL, 983, L40
Montet, B. T., Morton, T. D., Foreman-Mackey, D., et al. 2015, ApJ, 809, 25
T. pandas development team 2020, pandas-dev/pandas: Pandas, v3.0.1, Zenodo, doi:10.5281/zenodo.3509134
Perley, R. 2004, Wide-Field Imaging with the EVLA: WIDAR Correlator Modes and Output Data Rates Memo 64, National Radio Astronomy Observatory (NRAO) https://library.NRAO.edu/public/memos/evla/legacy/evlamemo64.pdf
Pica-Ciamarra, L., Madhusudhan, N., Cooke, G. J., Constantinou, S., & Binet, M. 2025, arXiv:2505.10539
Saide, R. C., Farah, W., Sheikh, S. Z., et al. 2023, RNAAS, 7, 233
Sarkis, P., Henning, T., Kürster, M., et al. 2018, AJ, 155, 257
Sheikh, S. Z., Kanodia, S., Lubar, E., et al. 2023, AJ, 165, 61
Sheikh, S. Z., Huston, M. J., Fan, P., et al. 2025, AJ, 169, 118
Siemion, A. P. V., Demorest, P., Korpela, E., et al. 2013, ApJ, 767, 94
Tremblay, C. D., Varghese, S. S., Hickish, J., et al. 2024, AJ, 167, 35
Tremblay, C. D., Sofair, J., Steffes, L., et al. 2025, AJ, 169, 122
Tsai, S.-M., Innes, H., Lichtenberg, T., et al. 2021, ApJ, 922L, L27
Tusay, N., Sheikh, S. Z., Sneed, E. L., et al. 2024, AJ, 168, 283
Wandia, K., Tremblay, C., Garrett, M. A., et al. 2026, MNRAS, 546, staf1998
Waskom, M. L. 2021, JOSS, 6, 3021
Welbanks, L., Nixon, M. C., McGill, P., et al. 2025, NatAs, in press
Wright, J. T., Haqq-Misra, J., Frank, A., et al. 2022, ApJL, 927, L30